Communications on Applied Mathematics and Computation
https://doi.org/10.1007/s42967-023-00291-9

ORIGINAL PAPER

Piecewise Acoustic Source Imaging with Unknown Speed of Sound Using a Level-Set Method

Guanghui Huang[1] · **Jianliang Qian**[2,3] · **Yang Yang**[3]

Received: 29 October 2022 / Revised: 2 April 2023 / Accepted: 18 May 2023

Abstract
We investigate the following inverse problem: starting from the acoustic wave equation, reconstruct a piecewise constant passive acoustic source from a single boundary temporal measurement without knowing the speed of sound. When the amplitudes of the source are known a priori, we prove a unique determination result of the shape and propose a level set algorithm to reconstruct the singularities. When the singularities of the source are known a priori, we show unique determination of the source amplitudes and propose a least-squares fitting algorithm to recover the source amplitudes. The analysis bridges the low-frequency source inversion problem and the inverse problem of gravimetry. The proposed algorithms are validated and quantitatively evaluated with numerical experiments in 2D and 3D.

Keywords Inverse gravimetry · Acoustic source imaging · Inversion of sound speed · Level-set method · Inverse problem

Mathematics Subject Classification 65N21 · 65N06 · 15A23 · 65F50 · 65R10

Dedicated to Prof. Stan Osher on the occasion of his 80th birthday.

✉ Jianliang Qian
jqian@msu.edu

Guanghui Huang
guanghui.huang@pgs.com

Yang Yang
yangy5@msu.edu

[1] Petroleum Geo-Services, Houston, TX 77079, USA

[2] Department of Mathematics, Michigan State University, East Lansing, MI 48824, USA

[3] Department of Computational Mathematics, Science and Engineering, Michigan State University, East Lansing, MI 48824, USA

Published online: 29 August 2023

1 Introduction

Passive acoustic source imaging is an exploration technique that uses naturally generated acoustic signals to image the interior of objects of interest. This technique has broad application in the areas of seismic and medical imaging. In seismology, passive seismic sources such as micro-earthquakes provide crucial information for reservoir monitoring and structural imaging. For instance, the localization of micro-seismic events is useful for understanding the extension of hydraulic fracturing [20]. In medical imaging, emerging coupled-physics modalities such as Photo-Acoustic Tomography (PAT) and Thermo-Acoustic Tomography (TAT) enable high-contrast high-resolution in-vivo imaging by triggering internal passive acoustic sources [51].

This paper concerns the inverse problem of imaging a passive acoustic source from a single measurement of the temporal wave field in a medium where the speed of sound information is unavailable. Specifically, letting $f(\mathbf{x})$ be a spatially varying function, we consider the acoustic wave propagation described by the following equation in the weak sense:

$$\frac{1}{c^2(\mathbf{x})}\frac{\partial^2 \hat{u}(t,\mathbf{x})}{\partial t^2} - \Delta \hat{u}(t,\mathbf{x}) = \delta(t) f(\mathbf{x}) \quad \text{in } \mathbb{R}\times\mathbb{R}^n, \tag{1}$$

$$\hat{u}(t,\mathbf{x})\big|_{t\leqslant 0} = 0. \tag{2}$$

Here $\hat{u} = \hat{u}(t,\mathbf{x})$ denotes the acoustic wave field generated by the spatially-varying source $f(\mathbf{x})$, $c(\mathbf{x})$ is the speed of sound (SOS), and $\delta(t)$ is the temporal Dirac-delta function. This equation models the propagation of acoustic waves generated by the instantaneous source f in the free space $\mathbb{R}^d$. Let Ω be the object of interest to be imaged. We assume that the wave is measured by transducers placed everywhere along the boundary $\partial\Omega$ to yield the temporal data

$$\{\hat{u}(t,\mathbf{z})\colon (t,\mathbf{z}) \in \mathbb{R}\times\partial\Omega\}. \tag{3}$$

We are interested in imaging the source f from the data (3) in the absence of knowledge of the SOS c. This inverse problem arises naturally in PAT and TAT; see Remark 1 for detailed discussion.

Other Works Inverse problems in passive acoustic source imaging have been extensively studied in the literature of seismic and medical imaging. The strategies can be classified into two categories based on the knowledge of SOS. When the SOS is known, this is a linear inverse problem and has been well understood. In particular, under a non-trapping condition for the SOS, it has been established that the source can be uniquely and stably determined [41]. In this case, effective numerical methods have been developed for source reconstruction. Typical algorithms include time reversal [2, 3, 5, 11, 19], Neumann series [6, 37, 41], and least squares fitting [40] with multi-frequency marching [4]. These methods rely on the knowledge of the SOS in an essential way to back propagate the boundary wave traces to retrieve the source.

When the SOS is unknown, joint reconstruction of the source and SOS pair (c, f) has been proposed in the literature. This problem raises more challenges, as the data (3) is nonlinear and non-convex as a functional of the SOS c. In the context of PAT and TAT, the linearized joint reconstruction problem is shown to be unstable in any scale of Sobolev spaces at sufficiently smooth pairs (c, f) [42]. For nonlinear joint reconstruction,

unique determination has been shown only for special pairs when $T = \infty$. These include radially symmetric SOS's in odd dimensions [8], and sources and/or SOS's that depend on fewer degrees of freedom [21, 30]. Numerical algorithms based on least-squares fitting have been developed for the joint reconstruction problem [12, 33, 38, 43, 48, 55]. A majority of these algorithms make use of non-convex optimizations to alternatively update the source and SOS. In each iteration, the SOS is updated via the full waveform inversion using the estimated source, and then the source is updated based on the estimated SOS using time reversal or back-propagation. On the other hand, a recent algorithm in [38] takes a different data-splitting approach for the joint reconstruction. The idea is to first isolate the information of the SOS from the source by taking the imaginary part of the data in the frequency domain. This results in a sourceless Helmholtz equation with known boundary data, in which the full waveform inversion is exploited to reconstruct the SOS; the source then can be acquired from time reversal or back-propagation. More results regarding joint reconstruction using other approaches can be found in [1, 39, 45, 53, 54]. See [9, 22–24] for recovering SOS by Eikonal-based traveltime tomography and [27] for recovering SOS and mass density contrast by joint inversion of traveltime and gravity data.

Our Contribution In this paper, we attempt to tackle the source imaging problem in a way different from the joint reconstruction: we are interested in recovering the source in the absence of the SOS information; that is, we consider passive acoustic source imaging in an unknown medium, where the spatial distribution of SOS is either inaccessible or costly to acquire. Scenarios where this situation occurs include earthquake localization and PAT/TAT in complex environment where the medium parameters are not fully available. In these applications, the objective is to identify the source but not the SOS. While using the SOS improves the accuracy of source imaging, it unavoidably gives rise to additional computational overhead, making source imaging less efficient. In contrast, the proposed method separates information of the source from that of the SOS, allowing standalone reconstruction of the source. See [38] for a related work. It is worth mentioning that our theoretical analysis shows that certain SOS's can be recovered independent of the source as well. This leads to new constructive methods for joint reconstruction. However, the resulting SOS inversion is less stable than the source inversion, posing more challenges to numerical implementations.

The sources of primary interest in this paper are the piecewise constant ones. Given the amplitudes of such a source, we prove that the singularities (hence the source itself) are uniquely determined. In this case, an algorithm based on the level set method [34, 35] is proposed for singularity reconstruction. Although our proof and numerical algorithm are based on the low-frequency assumption, the imaging resolution maybe high, which is not limited to the well-known diffraction limit (half of wavelength). This is mainly because we rely on the level-set representation of unknown objects, leading to a nonlinear geometric-domain inverse problem which may achieve high resolution. In addition, our algorithm is very stable with respect to the random noise. Numerical experiments are conducted in 2D and 3D to quantitatively evaluate the feasibility of the algorithm. On the other hand, given the singularities, we prove that the amplitudes (hence the source itself) are uniquely determined. These proofs provide a link to bridge the multi-frequency source inversion problem and another celebrated inverse problem known as the inverse gravimetry problem.

Paper Organization The paper is organized as follows. Section 2 discusses the formulation of the problem in the frequency domain, where we apply the low frequency asymptotics of the Helmholtz fundamental solution to obtain an expansion of

the gradient of the forward wave solution. Section 3 utilizes the expansion to establish connections with the inverse problem of gravimetry, and consequently proves the unique identifiability of piecewise constant sources and SOS's. Reconstruction algorithms based on the level set method are proposed and analyzed. Section 4 is devoted to the implementation and validation of the proposed reconstruction algorithms. Several numerical experiments in 2D and 3D are demonstrated to quantitatively evaluate the algorithmic accuracy and effectiveness using data from simulated photoacoustic tomography.

2 Frequency Domain Formulation and Low Frequency Asymptotics

While the problem formulation (1) and (3) is in the time domain, our method is designed in the frequency domain. Thus, we will take the temporal Fourier transform of the acoustic equation (1) to obtain the Helmholtz equation. The transformed data (3) will yield boundary data of the Helmholtz solution at all frequencies. A low-frequency asymptotic expansion is then exploited to isolate the source f from the SOS. We remark that the idea of using low-frequency asymptotic expansion to jointly determine multiple wave parameters goes back to [30]; see also [21].

We will make the following assumptions on the unknown parameters.

A1: the source f is compactly supported inside Ω; we denote the support by $\Omega_f \subset \Omega$.
A2: the SOS c differs from a constant background SOS c_0 only on a compact subset of Ω. In other words, if we define the relative squared slowness contrast function

$$r(\mathbf{x}) := \frac{c_0^2}{c^2(\mathbf{x})} - 1, \tag{4}$$

and denote its support by Ω_r, then $\Omega_r \subset \Omega$.
A3: the SOS c is sufficiently regular so that the forward problem (1) and (2) is well-posed.

2.1 Frequency Domain Formulation

In (1), we take the temporal Fourier transform of $u(\omega, \mathbf{x}) := \int_{-\infty}^{+\infty} \hat{u}(t, \mathbf{x}) \mathrm{e}^{\mathbf{i}\omega t} \mathrm{d}t$. The inverse Fourier transform is given by $\hat{u}(t, \mathbf{x}) = \frac{1}{2\pi} \int_{-\infty}^{+\infty} u(\omega, \mathbf{x}) \mathrm{e}^{-\mathbf{i}\omega t} \mathrm{d}\omega$. The acoustic wave equation (1) becomes the Helmholtz equation:

$$-\frac{\omega^2}{c^2(\mathbf{x})} u - \Delta u = f(\mathbf{x}) \quad \text{in } \mathbb{R}^d \tag{5}$$

subject to the Sommerfeld condition $|\mathbf{x}|^{\frac{d-1}{2}} \left(\frac{\partial}{\partial |\mathbf{x}|} u - \frac{\mathbf{i}\omega}{c_0(\mathbf{x})} u \right) \to 0$ as $|\mathbf{x}| \to +\infty$. Under the Fourier transform, the temporal data (3) is transformed to the frequency-domain data

$$\{u(\omega, \mathbf{z}) \colon \omega \in \mathbb{R}, \ \mathbf{z} \in \partial\Omega\}. \tag{6}$$

The inverse problem formulated in the frequency domain seeks to image f in (5) from the multi-frequency data (6).

We can utilize the boundary value (6) to obtain the full Cauchy data on $\partial\Omega$. Indeed, as $f(\mathbf{x})$ and $c(\mathbf{x}) - c_0(\mathbf{x})$ are compactly supported in Ω, the Helmholtz equation (5) restricted to the exterior domain $\mathbb{R}^d \backslash \overline{\Omega}$ reads

$$-\frac{\omega^2}{c_0^2(\mathbf{x})} u - \Delta u = 0 \quad \text{in } \mathbb{R}^d \backslash \overline{\Omega}$$

subject to the Sommerfeld condition at infinity. Given the data (6), we can solve the boundary value problem in $\mathbb{R}^d \backslash \overline{\Omega}$ to obtain the boundary gradient data:

$$\{\nabla_{\mathbf{z}} u(\omega, \mathbf{z}) \colon \omega \in \mathbb{R},\ \mathbf{z} \in \partial\Omega\}. \tag{7}$$

From now on, we will assume the availability of both the boundary data (6) and the boundary gradient (7), which put together are equivalent to the Cauchy data at $\partial\Omega$.

Remark 1 An application of the inverse problem in consideration is to PAT and TAT. PAT and TAT are emerging multi-wave modalities that combine multiple types of waves to achieve high-contrast, high-resolution imaging. In PAT/TAT, electromagnetic radiation such as laser/microwave is sent to illuminate biological tissue to generate instantaneous acoustic sources inside biological tissue through the photoacoustic effect. Let $p(t, \mathbf{x})$ be the acoustic pressure at time t and location $\mathbf{x}$, and the variation of the acoustic pressure in PAT and TAT satisfies the equation [49, 50, 52]:

$$\begin{cases} \frac{1}{c^2(\mathbf{x})} \frac{\partial^2 p(t,\mathbf{x})}{\partial t^2} - \Delta p(t, \mathbf{x}) = 0 & \text{in } (0, +\infty) \times \mathbb{R}^d, \\ p(0, \mathbf{x}) = p_0(\mathbf{x}), \\ \frac{\partial p}{\partial t}(0, \mathbf{x}) = 0. \end{cases} \tag{8}$$

Here $p_0(\mathbf{x})$ is the spatial distribution of the instantaneous acoustic source. The PAT and TAT measurement is

$$\{p(t, \mathbf{z}) \colon (t, \mathbf{z}) \in [0, T] \times \partial\Omega\}, \tag{9}$$

where $T > 0$ is the duration of measurement. The inverse problem in PAT and TAT aims to image the initial source p_0 from the boundary measurement (9).

We can transform the PAT/TAT model (8) and data (9) as follows. First, defining $\hat{v}(t, \mathbf{x}) := \int_0^t p(\tau, \mathbf{x})\, \mathrm{d}\tau$, $\hat{v}$ satisfies

$$\begin{cases} \frac{1}{c^2(\mathbf{x})} \frac{\partial^2 \hat{v}(t,\mathbf{x})}{\partial t^2} - \Delta \hat{v}(t, \mathbf{x}) = 0 & \text{in } (0, +\infty) \times \mathbb{R}^d, \\ \hat{v}(0, \mathbf{x}) = 0, \\ \frac{\partial \hat{v}}{\partial t}(0, \mathbf{x}) = p_0. \end{cases} \tag{10}$$

Next, let $\hat{u} = \hat{u}(t, \mathbf{x})$ be the zero extension of $\hat{v}$ to $\mathbb{R} \times \mathbb{R}^d$. Integration by parts using (10) shows that $\hat{u}$ satisfies the conditions (1)–(2) in the weak sense with $f(\mathbf{x}) := \frac{p_0(\mathbf{x})}{c^2(\mathbf{x})}$. As a result, our method provides a numerical algorithm to image the ratio of the source p_0 and the underlying velocity c in PAT/TAT in the absence of knowledge of p_0 and c.

Introduce the reference wave number $k := \frac{\omega}{c_0}$ and write the Helmholtz equation (5) as

$$(\Delta + k^2)u = -f - k^2 ru.$$

Recall that the supports of f and r (see (4) for the definition of r) are denoted by Ω_f and Ω_r respectively, with $\Omega_f \subset \Omega$ and $\Omega_r \subset \Omega$. The celebrated Lippmann-Schwinger equation gives

$$u(k,\mathbf{x}) = \int_{\Omega_f} G_k(\mathbf{x},\mathbf{y}) f(\mathbf{y}) \mathrm{d}\mathbf{y} + k^2 \int_{\Omega_r} G_k(\mathbf{x},\mathbf{y}) r(\mathbf{y}) u(k,\mathbf{y}) \mathrm{d}\mathbf{y}, \ \mathbf{x} \in \mathbb{R}^d \backslash (\Omega_f \cup \Omega_r). \quad (11)$$

Here $G_k(\mathbf{x},\mathbf{y})$ is the fundamental solution of the Helmholtz equation, that is, $(\Delta + k^2) \cdot G_k(\mathbf{x},\mathbf{y}) = -\delta_{\mathbf{y}}(\mathbf{x})$ in $\mathbb{R}^d$. It can be explicitly represented as

$$G_k(\mathbf{x},\mathbf{y}) = \begin{cases} \frac{\mathbf{i}}{4} H_0^{(1)}(k|\mathbf{x}-\mathbf{y}|) & \text{in 2D}, \\ \frac{\mathrm{e}^{\mathbf{i}k|\mathbf{x}-\mathbf{y}|}}{4\pi|\mathbf{x}-\mathbf{y}|} & \text{in 3D}, \end{cases} \quad (12)$$

where $H_0^{(1)}$ is the Hankel function of the first kind of order 0. The solution u is known as the scattering wave in literature.

Remark 2 Note that the above derivation for $d = 3$ extends easily to higher dimensions $d \geqslant 3$; see [30]. The discussion in this paper is restricted to $d = 2, 3$ so as to be consistent with the computational work shown in later sections.

2.2 Low Frequency Asymptotics

We will study the asymptotic expansion of $u(k,\mathbf{x})$ in (11) near $k = 0$. This is motivated by the observation that only the first integral in (11) involves $O(1)$ and $O(k)$-terms, and thus can be utilized to isolate information regarding f in the absence of knowledge of c.

Henceforth, we write $G_0(\mathbf{x},\mathbf{y})$ for the fundamental solution of the Laplace equation, that is, $\Delta G_0(\mathbf{x},\mathbf{y}) = -\delta_{\mathbf{y}}(\mathbf{x})$ in $\mathbb{R}^d$. The explicit representation is

$$G_0(\mathbf{x},\mathbf{y}) = \begin{cases} -\frac{1}{2\pi} \ln(|\mathbf{x}-\mathbf{y}|) & \text{in 2D}, \\ \frac{1}{4\pi|\mathbf{x}-\mathbf{y}|} & \text{in 3D}. \end{cases} \quad (13)$$

Then the integral representation of the Laplace solution with the source function $f(\mathbf{x})$ is given by $u_0(\mathbf{x}) = \int_{\mathbb{R}^d} G_0(\mathbf{x},\mathbf{y}) f(\mathbf{y}) \mathrm{d}\mathbf{y}$. It is well known that $u_0(\mathbf{x})$ serves as an approximate solution of the scattering solution to (5) at the zero frequency $k = 0$ (or equivalently, $\omega = 0$). Next, in order to find higher order approximations, we will derive the asymptotic expansion of the scattering solution $u(k,\mathbf{x})$ near $k = 0$ using its analyticity with respect to the frequency k.

Lemma 1 *Let $u(k,\mathbf{x})$ be the scattering solution of (5) with $k = \frac{\omega}{c_0}$. For a sufficiently small wave number k, we have the following low frequency expansion*:

$$\nabla_{\mathbf{x}} u(k,\mathbf{x}) = \begin{cases} \nabla_{\mathbf{x}} u_0(\mathbf{x}) + k^2 \left(\nabla_{\mathbf{x}} u_2^r(\mathbf{x}) + \mathbf{i} \nabla_{\mathbf{x}} u_2^i(\mathbf{x}) \right) + O(k^4 \ln(k)) & \text{in } 2D, \\ \nabla_{\mathbf{x}} u_0(\mathbf{x}) + k^2 \nabla_{\mathbf{x}} u_2(\mathbf{x}) + \mathbf{i} k^3 \nabla_{\mathbf{x}} u_3(\mathbf{x}) + O(k^4) & \text{in } 3D, \end{cases} \quad (14)$$

which holds uniformly for $\mathbf{x} \in \partial\Omega$. Here the functions $u_0, \cdots, u_3$ can be explicitly represented in terms of f and c. In particular, we have in 2D,

$$\nabla_{\mathbf{x}} u_0(\mathbf{x}) = \int_{\Omega_f} \nabla_{\mathbf{x}} G_0(\mathbf{x}, \mathbf{y}) f(\mathbf{y}) \mathrm{d}\mathbf{y}, \tag{15}$$

$$\nabla_{\mathbf{x}} u_2^i(\mathbf{x}) = -\frac{1}{8} \int_{\Omega_f} (\mathbf{x} - \mathbf{y}) f(\mathbf{y}) \mathrm{d}\mathbf{y} + u_1 \int_{\Omega_r} \nabla_{\mathbf{x}} G_0(\mathbf{x}, \mathbf{y}) r(\mathbf{y}) \mathrm{d}\mathbf{y}. \tag{16}$$

In 3D, we have

$$\nabla_{\mathbf{x}} u_0(\mathbf{x}) = \int_{\Omega_f} \nabla_{\mathbf{x}} G_0(\mathbf{x}, \mathbf{y}) f(\mathbf{y}) \mathrm{d}\mathbf{y}, \tag{17}$$

$$\nabla_{\mathbf{x}} u_3(\mathbf{x}) = -\frac{1}{12\pi} \int_{\Omega_f} (\mathbf{x} - \mathbf{y}) f(\mathbf{y}) \mathrm{d}\mathbf{y} + u_1 \int_{\Omega_r} \nabla_{\mathbf{x}} G_0(\mathbf{x}, \mathbf{y}) r(\mathbf{y}) \mathrm{d}\mathbf{y}. \tag{18}$$

Proof We first consider the three dimensional case. Suppose the scattering solution $u(k, \mathbf{x})$ admits an expansion

$$u(\omega, \mathbf{x}) = u_0(\mathbf{x}) + \mathbf{i}k u_1(\mathbf{x}) + k^2 u_2(\mathbf{x}) + \mathbf{i}k^3 u_3(\mathbf{x}) + \cdots. \tag{19}$$

As the fundamental solution $G_k(\mathbf{x}, \mathbf{y})$ has the following expansion [7]:

$$G_k(\mathbf{x}, \mathbf{y}) = \frac{1}{4\pi|\mathbf{x} - \mathbf{y}|} \left(1 + \mathbf{i}k|\mathbf{x} - \mathbf{y}| - \frac{k^2}{2}|\mathbf{x} - \mathbf{y}|^2 - \frac{\mathbf{i}k^3}{6}|\mathbf{x} - \mathbf{y}|^3\right) + O(k^4), \tag{20}$$

we can insert these expansions of u and G_k into the Lippmann-Schwinger equation (11) and compare the orders of k to obtain

$$u_0(\mathbf{x}) = \int_{\Omega_f} G_0(\mathbf{x}, \mathbf{y}) f(\mathbf{y}) \mathrm{d}\mathbf{y}, \tag{21}$$

$$u_1(\mathbf{x}) = \frac{1}{4\pi} \int_{\Omega_f} f(\mathbf{y}) \mathrm{d}\mathbf{y}, \tag{22}$$

$$u_2(\mathbf{x}) = -\frac{1}{8\pi} \int_{\Omega_f} |\mathbf{x} - \mathbf{y}| f(\mathbf{y}) \mathrm{d}\mathbf{y} + \int_{\Omega_r} G_0(\mathbf{x}, \mathbf{y}) r(\mathbf{y}) u_0(\mathbf{y}) \mathrm{d}\mathbf{y}, \tag{23}$$

$$u_3(\mathbf{x}) = -\frac{1}{24\pi} \int_{\Omega_f} |\mathbf{x} - \mathbf{y}|^2 f(\mathbf{y}) \mathrm{d}\mathbf{y} + \int_{\Omega_r} G_0(\mathbf{x}, \mathbf{y}) r(\mathbf{y}) u_1(\mathbf{y}) \mathrm{d}\mathbf{y} + \frac{1}{4\pi} \int_{\Omega_r} r(\mathbf{y}) u_0(\mathbf{y}) \mathrm{d}\mathbf{y}. \tag{24}$$

Taking the gradient of these functions yields the desired expansion in 3D as well as the representations (17)–(18). Note that $\nabla_{\mathbf{x}} u_1 \equiv 0$ since u_1 is constant.

Next, we consider the two dimensional case. Let the scattering solution $u(\omega, \mathbf{x})$ be of the form

$$u(k,\mathbf{x}) = \tilde{u}_0(\mathbf{x}) + \mathbf{i}ku_1(\mathbf{x}) + k^2u_2(\mathbf{x}) + \cdots. \tag{25}$$

In 2D, the fundamental solution $G_k(\mathbf{x},\mathbf{y})$ has the following expansion [7]:

$$\begin{aligned} G_k(\mathbf{x},\mathbf{y}) = &-\frac{1}{2\pi}\Big(\ln(|\mathbf{x}-\mathbf{y}|) + \ln\frac{k}{2} + C\Big) + \frac{\mathbf{i}}{4} - \frac{\mathbf{i}}{16}k^2|\mathbf{x}-\mathbf{y}|^2 \\ &+ \frac{k^2|\mathbf{x}-\mathbf{y}|^2}{8\pi}\Big(\ln(|\mathbf{x}-\mathbf{y}|) + \ln\frac{k}{2} + C_r - 1\Big) + O(k^4\ln k), \end{aligned} \tag{26}$$

where $C_r = 0.577\,211\cdots$ is Euler's constant. Similar to the three dimensional case, we plug both (25) and (26) into (11) to yield

$$\tilde{u}_0(\mathbf{x}) = u_0(\mathbf{x}) - \frac{1}{2\pi}\Big(\ln\frac{k}{2} + C_r\Big)\int_{\Omega_f} f(\mathbf{y})\mathrm{d}\mathbf{y}, \tag{27}$$

$$u_1(\mathbf{x}) = \frac{1}{4}\int_{\Omega_f} f(\mathbf{y})\mathrm{d}\mathbf{y}, \tag{28}$$

$$\begin{aligned} u_2^r(\mathbf{x}) = &\int_{\Omega_f} \frac{|\mathbf{x}-\mathbf{y}|^2}{8\pi}\Big(\ln(|\mathbf{x}-\mathbf{y}|) + \ln\frac{k}{2} + C_r - 1\Big)f(\mathbf{y})\mathrm{d}\mathbf{y} \\ &- \int_{\Omega_r}\Big(\Big(\frac{1}{2\pi}\ln\frac{k|\mathbf{x}-\mathbf{y}|}{2} + C_r\Big)\tilde{u}_0(\mathbf{y}) + \frac{1}{4}r(\mathbf{y})u_1(\mathbf{y})\Big)\mathrm{d}\mathbf{y}, \end{aligned} \tag{29}$$

$$\begin{aligned} u_2^i(\mathbf{x}) = &-\int_{\Omega_f}\frac{|\mathbf{x}-\mathbf{y}|^2}{16}f(\mathbf{y})\mathrm{d}\mathbf{y} + \int_{\Omega_r} G_0(\mathbf{x},\mathbf{y})r(\mathbf{y})u_1(\mathbf{y})\mathrm{d}\mathbf{y} \\ &- \frac{1}{2\pi}\Big(\ln\frac{k}{2} + C_r\Big)\int_{\Omega_r} r(\mathbf{y})u_1(\mathbf{y})\mathrm{d}\mathbf{y} + \frac{1}{4}\int_{\Omega_r} r(\mathbf{y})\tilde{u}_0(\mathbf{y})\mathrm{d}\mathbf{y}, \end{aligned} \tag{30}$$

where $u_0(\mathbf{x}) := \int_{\Omega_f} G_0(\mathbf{x},\mathbf{y})f(\mathbf{y})\mathrm{d}\mathbf{y} = -\frac{1}{2\pi}\int_{\Omega_f}\ln(|\mathbf{x}-\mathbf{y}|)f(\mathbf{y})\mathrm{d}\mathbf{y}$, and u_2^r and u_2^i denote the real part and the imaginary part of u_2, respectively. Taking the gradient of these functions yields the desired expansion in 2D as well as the representations (15)–(16). Note that $\nabla_{\mathbf{x}}u_0 = \nabla_{\mathbf{x}}\tilde{u}_0$ by the definition of u_0.

Remark 3 Given the explicit forms of u_0, u_1, u_2, and u_3, the following conclusions are straightforward in 3D.

i. We take the divergence of (17) to obtain

$$\Delta u_0 = -f\chi(\Omega_f),$$

where $\chi(\Omega_f)$ is the characteristic function of Ω_f. Consequently, if φ is a harmonic function in Ω, that is, $\Delta\varphi = 0$ in Ω, then

$$-\int_{\Omega_f}\varphi(\mathbf{x})f(\mathbf{x})\mathrm{d}\mathbf{x} = \int_{\Omega}\varphi(\mathbf{x})\Delta u_0(\mathbf{x})\mathrm{d}\mathbf{x} = \int_{\partial\Omega}\big(\varphi(\mathbf{z})\partial_\nu u_0(\mathbf{z}) - \partial_\nu\varphi(\mathbf{z})u_0(\mathbf{z})\big)\mathrm{d}s_{\mathbf{z}}.$$

As the boundary values and normal derivatives of φ and u_0 are known, one can determine the integral on the left-hand side. This recovers [30, Theorem 2.1].

ii. We take the divergence of (18) to obtain

$$\Delta u_3(\mathbf{x}) = -\frac{1}{4\pi}\int_{\Omega_f} f(\mathbf{y})\mathrm{d}\mathbf{y} - u_1 r(\mathbf{x}) = -u_1(1 + r(\mathbf{x})).$$

Consequently, if φ is a harmonic function in Ω, that is, $\Delta\varphi = 0$ in Ω, then

$$-u_1\int_\Omega (1 + r(\mathbf{x}))\varphi(\mathbf{x})\mathrm{d}\mathbf{x} = \int_\Omega \varphi(\mathbf{x})\Delta u_3(\mathbf{x})\mathrm{d}\mathbf{x} = \int_{\partial\Omega}\big(\varphi(\mathbf{z})\partial_\nu u_3(\mathbf{z}) - \partial_\nu\varphi(\mathbf{z})u_3(\mathbf{z})\big)\mathrm{d}s_{\mathbf{z}}.$$

As the boundary values and normal derivatives of φ and u_3 are known, one can determine the following integral if the constant $u_1 \neq 0$:

$$\int_\Omega (1 + r(\mathbf{x}))\varphi(\mathbf{x})\mathrm{d}\mathbf{x} = c_0^2\int_\Omega \frac{1}{c^2(\mathbf{x})}\varphi(\mathbf{x})\mathrm{d}s_{\mathbf{x}},$$

where we have used the definition of $r(\mathbf{x})$, (4). As the background constant velocity c_0 is known, this recovers [21, Theorem 1.1].

These results can be proved in 2D likewise when $u_3(\mathbf{x})$ is replaced by $u_2^i(\mathbf{x})$.

3 Uniqueness and Reconstruction of Piecewise Constant Sources and Velocities

In the following sections, we will be concerned with reconstruction of piecewise constant sources and velocities. For general sources and velocities (i.e., not necessarily piecewise constant), we believe that the reconstruction may yield a piecewise constant approximation that corresponds to the data due to some equivalent source, since the ultra-low frequency assumption renders our current inverse problem close to the regime of inverse source problems of gravimetry. This subtle point can be seen from some examples shown in [26, 32], which have treated data arising from the setup which does not satisfy the required assumptions of uniqueness theorems; our experience in inverse source problems of gravimetry [32] and magnetics [26] indicates that our level-set based algorithms will yield some reconstruction results corresponding to some equivalent sources which do satisfy the assumptions needed for the uniqueness theorems to hold.

3.1 The Inverse Problem of Gravimetry

We recall the inverse problem of gravimetry in this subsection and point out its connection with our problem. Let $g(\mathbf{x})$ be a mass distribution that is compactly supported inside a domain Ω, and the gravitational field $U(\mathbf{x})$ generated by g satisfies the Poisson equation ($d = 2, 3$)

$$\Delta U(\mathbf{x}) = -g(\mathbf{x}) \qquad \text{in } \mathbb{R}^d$$

with the condition that $U(\mathbf{x}) \to 0$ as $|\mathbf{x}| \to \infty$. The inverse problem of gravimetry concerns reconstruction of the distribution $g(\mathbf{x})$ from the resulting gravitational force $\nabla_{\mathbf{x}} U(\mathbf{x})$ measured at the boundary $\partial\Omega$. Using the fundamental solution $G_0(\mathbf{x}, \mathbf{y})$ of the Laplacian, the gravitational force admits the representation

$$\nabla_{\mathbf{x}} U(\mathbf{x}) = \int_{\Omega} \nabla_{\mathbf{x}} G_0(\mathbf{x}, \mathbf{y}) g(\mathbf{y}) \mathrm{d}\mathbf{y}.$$

This problem was formulated by Laplace, and the first results were obtained by Stokes in the 1860s and Herglotz in 1910s [10]. In general, $g(\mathbf{x})$ cannot be uniquely determined by the boundary gravitational force $\nabla_{\mathbf{x}} U|_{\partial\Omega}$, as the former has more degrees of freedom than the latter. On the other hand, uniqueness and stability results have been established for some special classes of functions $g(\mathbf{x})$ under suitable assumptions. Detailed analysis of the problem and survey of more recent results are available in the books [15, 16].

In particular, we consider the function $g(\mathbf{x})$ which is piecewise constant of the form

$$g(\mathbf{x}) = \sum_{j=1}^{N} g_j \chi(\Omega_j), \tag{31}$$

where g_j is a constant, $\{\Omega_j\}$'s are disjoint subdomains with smooth boundary such that $\cup_{j=1}^{N} \Omega_j \subset \Omega$, and $\chi(\Omega_j)$ is the characteristic function of Ω_j. If the amplitudes g_j's are known a priori, then the subdomains Ω_j's can be uniquely determined. We record this uniqueness result due to Isakov [15, Theorem 3.1.1].

Theorem 1 [15, Theorem 3.1.1] *Suppose the domain Ω consists of multiple star-shaped subdomains Ω_j with respect to their centers of gravity, and $g(\mathbf{x})$ takes a constant value g_j that is known a priori on each subdomain Ω_j. Under these assumptions, all the subdomains Ω_j's are uniquely determined by the boundary gravimetric data $\nabla_{\mathbf{x}} U(\mathbf{x})|_{\partial\Omega}$.*

On the other hand, if the subdomains Ω_j's are known a priori, Isakov proved that the constant amplitudes g_j's can be uniquely determined [15, Theorem 3.3.1].

Theorem 2 [15, Theorem 3.3.1] *Suppose the domain Ω consists of multiple connected subdomains Ω_j with smooth boundary, and $g(\mathbf{x})$ takes a constant value g_j on each subdomain Ω_j. If Ω_j's are known a priori, then all the values g_j's are uniquely determined by the boundary gravimetric data $\nabla_{\mathbf{x}} U(\mathbf{x})|_{\partial\Omega}$.*

3.2 Uniqueness of Piecewise Constant Sources and Velocities

Combining Theorem 1, Theorem 2, and the representations (15) and (17), we obtain the following uniqueness result for the reconstruction of piecewise constant sources without the velocity information if the source amplitudes are known a priori.

Theorem 3 (Identification of piecewise constant sources) *Let the source function $f(\mathbf{x})$ be a piecewise constant function of the form*

$$f(\mathbf{x}) = \sum_{j=1}^{N_f} f_j \chi(\Omega_{f_j})$$

with disjoint connected supports Ω_{f_j}.

(i) *If the subdomains* Ω_{f_j}*'s are star-shaped with respect to their centers of gravity and the constant amplitudes* f_j *are known, then the sets* $\{\Omega_{f_j}\}_{j=1}^{N_f}$ *are uniquely determined.*
(ii) *If the subdomains* Ω_{f_j}*'s are known, then the constant amplitudes* f_j *are uniquely determined.*

Proof Let $u(k, \mathbf{x})$ be the Helmholtz solution of (5) with $k = \frac{\omega}{c_0}$. By Lemma 1, we have

$$\lim_{k\to 0} \nabla_{\mathbf{x}} u(k, \mathbf{x}) = \nabla_{\mathbf{x}} u_0(\mathbf{x}) = \int_{\Omega_f} \nabla_{\mathbf{x}} G_0(\mathbf{x}, \mathbf{y}) f(\mathbf{y}) \mathrm{d}\mathbf{y}, \quad \mathbf{x} \in \partial\Omega_\rho$$

in either 2D or 3D. Note that the left-hand side $\lim_{\omega\to 0} \nabla_{\mathbf{x}} u(\omega, \mathbf{x})$ can be computed using the boundary Cauchy data of $u(\omega, \mathbf{x})$. If all the subdomains Ω_{f_j} are star-shaped with respect to the centers of gravity and f_j's are given, Theorem 1 asserts that the subdomains $\{\Omega_{f_j}\}$'s can be uniquely determined. If the subdomains $\{\Omega_{f_j}\}$'s are given, Theorem 2 asserts that the amplitudes f_j can be uniquely determined.

The idea can be further extended to uniquely determine a piecewise constant slowness contrast $r(\mathbf{x})$ in the absence of the knowledge of the source $f(\mathbf{x})$.

Theorem 4 (Identification of piecewise constant velocities) *Suppose the unknown source* f *satisfies* $\int_{\Omega_f} f(\mathbf{y})\mathrm{d}\mathbf{y} \neq 0$. *Let* $c(\mathbf{x})$ *be a piecewise constant velocity of the form*

$$c^2(\mathbf{x}) = c_0^2 + \sum_{j=1}^{N_c} c_j^2 \chi(\Omega_{c_j})$$

with disjoint connected supports Ω_{c_j}. *Here,* c_0 *is a known background velocity and* $c > 0$ *everywhere.*

(i) *If the subdomains* Ω_{c_j}*'s are star-shaped with respect to their centers of gravity and the constant amplitudes* Ω_{c_j} *are known, then the sets* $\{\Omega_{c_j}\}_{j=1}^{N_c}$ *are uniquely determined.*
(ii) *If the subdomains* Ω_{c_j}*'s are known, then the constant amplitudes* Ω_{c_j} *are uniquely determined.*

Proof Given the piecewise constant velocity, the slowness contrast

$$r = \frac{c_0^2}{c^2} - 1 = \sum_{j=1}^{N_c} r_j \chi(\Omega_{c_j}), \qquad r_j := -\frac{c_j^2}{c_0^2 + c_j^2}$$

is piecewise constant as well. Let $u(k, \mathbf{x})$ be the Helmholtz solution of (5) with $k = \frac{\omega}{c_0}$.

First, we prove the statements in 3D. By Lemma 1, we have for $\mathbf{x} \in \partial\Omega$ that

$$\begin{aligned}\lim_{k\to 0} \frac{1}{6\mathbf{i}} \partial_k^3 \big(\nabla_{\mathbf{x}} u\big)(\mathbf{x}) &= \nabla_{\mathbf{x}} u_3(\mathbf{x}) \\ &= -\frac{1}{12\pi} \int_{\Omega_f} (\mathbf{x} - \mathbf{y}) f(\mathbf{y}) \mathrm{d}\mathbf{y} + u_1 \int_{\Omega_r} \nabla_{\mathbf{x}} G_0(\mathbf{x}, \mathbf{y}) r(\mathbf{y}) \mathrm{d}\mathbf{y} \quad \text{in 3D.}\end{aligned} \tag{32}$$

Note that the left-hand side of (32) is known from the data for $\mathbf{x} \in \partial\Omega$. For the first term on the right-hand side, as $-\Delta u_0 = f\chi(\Omega_f)$, we apply the Green's Theorem to obtain

$$\int_{\Omega_f} (\mathbf{x} - \mathbf{y}) f(\mathbf{y}) \mathrm{d}\mathbf{y} = -\int_{\partial\Omega} \Big((\mathbf{x} - \mathbf{z}) \frac{\partial}{\partial \nu} u_0(\mathbf{z}) + u_0(\mathbf{z}) \nu \Big) \mathrm{d}s_{\mathbf{z}},$$

which is known from the data. Here ν denotes the exterior normal vector field to the boundary $\partial\Omega_\rho$. For the second term on the right-hand side of (32), we use the definition of u_1 and integration by parts:

$$\begin{aligned} u_1 &= \frac{1}{4\pi} \int_{\Omega_f} f(\mathbf{y}) \mathrm{d}\mathbf{y} = -\frac{1}{4\pi} \int_{\Omega} \Delta u_0(\mathbf{y}) \mathrm{d}\mathbf{y} \\ &= -\frac{1}{4\pi} \int_{\partial\Omega} \frac{\partial}{\partial \nu} u_0(\mathbf{z}) \mathrm{d}s_z = -\frac{1}{4\pi} \lim_{k\to 0} \int_{\partial\Omega} \frac{\partial}{\partial \nu} u(k, \mathbf{z}) \mathrm{d}s_{\mathbf{z}}, \end{aligned}$$

which is known from the data. Therefore, we can compute the integral

$$\int_{\Omega_r} \nabla_{\mathbf{x}} G_0(\mathbf{x}, \mathbf{y}) r(\mathbf{y}) \mathrm{d}\mathbf{y}, \qquad \mathbf{x} \in \partial\Omega.$$

This is another inverse problem of gravimetry for $r(\mathbf{x})$. Under the assumption of the theorem, Theorem 1 and Theorem 2 imply that the piecewise constant function $r(\mathbf{x})$ can be uniquely determined. The conclusion follows since $c^2 = \frac{c_0^2}{1+r}$.

The proof in 2D is similar: we use (16) in Lemma 1 instead to obtain for $\mathbf{x} \in \partial\Omega$ that

$$\begin{aligned}\lim_{k\to 0} \frac{1}{2} \partial_k^2 \, \mathrm{Im}\big(\nabla_{\mathbf{x}} u\big)(\mathbf{x}) &= \nabla_{\mathbf{x}} u_2^i(\mathbf{x}) \\ &= -\frac{1}{8} \int_{\Omega_f} (\mathbf{x} - \mathbf{y}) f(\mathbf{y}) \mathrm{d}\mathbf{y} + u_1 \int_{\Omega_r} \nabla_{\mathbf{x}} G_0(\mathbf{x}, \mathbf{y}) r(\mathbf{y}) \mathrm{d}\mathbf{y} \quad \text{in 2D.}\end{aligned} \tag{33}$$

The rest of the proof is identical to the three dimensional case.

3.3 Reconstruction Algorithm

Note that Theorem 3 ensures the uniqueness of piecewise constant sources regardless of the velocity information, and Theorem 4 ensures the uniqueness of piecewise constant slowness contrast functions regardless of the source information. In this section, we will provide numerical algorithms to reconstruct the source and velocity. For the source, we assume that it is piecewise constant with known amplitudes and unknown supports; for the velocity, we assume that it is piecewise constant with known supports and unknown amplitudes.

Suppose the piecewise constant source function f is

$$f(\mathbf{x}) = \sum_{j=1}^{N_f} f_j \chi(\Omega_{f_j}), \qquad \Omega_{f_j} \cap \Omega_{f_k} = \varnothing \text{ for } j \neq k.$$

If the source amplitudes $\{f_j\}$ are given a priori, we can parameterize the domain Ω_{f_j} by a level-set function ϕ_j with [35]

$$\begin{cases} \phi_j(\mathbf{x}) > 0 & \text{if} \quad \mathbf{x} \in \Omega_{f_j}, \\ \phi_j(\mathbf{x}) = 0 & \text{if} \quad \mathbf{x} \in \partial\Omega_{f_j}, \\ \phi_j(\mathbf{x}) < 0 & \text{if} \quad \mathbf{x} \in \Omega \backslash \overline{\Omega_{f_j}}. \end{cases}$$

Then $f(\mathbf{x}) = \sum_{j=1}^{N_f} f_j H(\phi_j(\mathbf{x}))$, where $H(t)$ is the Heaviside function

$$H(t) = \begin{cases} 1 & \text{if} \quad t > 0, \\ 0.5 & \text{if} \quad t = 0, \\ 0 & \text{if} \quad t < 0. \end{cases}$$

Denote the low frequency data $d := \lim_{\omega \to 0} \nabla_{\mathbf{x}} u(\omega, \mathbf{x})$ and the level-set representation

$$w(\mathbf{x}) := \sum_{j=1}^{N_f} f_j \int_{\mathbb{R}^d} \nabla_{\mathbf{x}} G_0(\mathbf{x}, \mathbf{y}) H(\phi_j(\mathbf{y})) \mathrm{d}\mathbf{y}, \quad \mathbf{x} \in \partial\Omega. \tag{34}$$

To find the associated level-set functions ϕ_j, we will minimize the data misfit between the simulated data w and measured data d according to the proof of Theorem 3 in the least-squares sense:

$$J[\phi_1, \phi_2, \cdots, \phi_{N_f}] = \frac{1}{2} \int_{\partial\Omega} |w(\mathbf{x}) - d(\mathbf{x})|^2 \mathrm{d}s(\mathbf{x}). \tag{35}$$

The gradient of this objective functional with respect to the j-th level-set fucntion ϕ_j is [17],

$$\nabla_{\phi_j} J[\phi_1, \phi_2, \cdots, \phi_{N_f}](\mathbf{x}) = f_j \delta(\phi_j(\mathbf{x})) \int_{\partial\Omega} \nabla_{\mathbf{z}} G_0(\mathbf{z}, \mathbf{x}) \big(w(\mathbf{z}) - d(\mathbf{z})\big) \mathrm{d}s(\mathbf{z}), \tag{36}$$

where δ is the Dirac delta function, and the data residual $w - d$ serves as the adjoint source that is back-propagated into the domain for updating the level-set functions.

We introduce an artificial time parameter t to drive the following evolution (Hamilton-Jacobi) equation to the steady state [17] by solving the equation with essentially non-oscillatory schemes [36]:

$$\frac{\partial}{\partial t}\phi_j(t,\mathbf{x}) = -\nabla_{\phi_j} J[\phi_1,\phi_2,\cdots,\phi_{N_f}](\mathbf{x}) \tag{37}$$

equipped with the Neumann boundary condition $\frac{\partial \phi_j}{\partial n}|_{\partial\Omega} = 0$ and the initial condition $\phi_j(0,\mathbf{x}) = \phi_{j,0}(\mathbf{x})$. Then the minimizer $\phi_j^*(\mathbf{x})$ of the least-squares objective functional (35) is given by $\phi_j^*(\mathbf{x}) = \lim_{t\to+\infty}\phi_j(t,\mathbf{x})$ [17]. We refer readers to [26, 47] for more details about numerical implementation of the multiple level-set method. We also refer readers to [25, 27–29, 32] for more recent works on using the level-set method for gravity inverse problems.

We summarize the algorithm to reconstruct piecewise constant sources without velocity information in Algorithm 1.

Algorithm 1 Level-set reconstruction of piecewise constant sources without velocity

i. Choose a small enough angular frequency ω_0 such that the input data can be approximated by $d(\mathbf{x}_r) \approx u(\mathbf{x},\omega) = \int_0^{+\infty} u(\mathbf{x},t)\mathrm{e}^{-\mathbf{i}\omega_0 t}\mathrm{d}t$. Given are the source amplitudes $f_1, f_2, \cdots, f_{N_f}$ and the corresponding initial guesses $\phi_{1,0}(\mathbf{x}), \phi_{2,0}(\mathbf{x}), \cdots, \phi_{N_f,0}(\mathbf{x})$.

ii. Evolve the following level-set equation to the steady state equation:

$$\frac{\partial}{\partial t}\phi_j(\mathbf{x},t) = -\nabla_{\phi_j} J[\phi_1,\phi_2,\cdots,\phi_{N_f}](\mathbf{x}) \tag{38}$$

with the initial condition and the Neumann boundary condition as above. Here, the gradient $\nabla_{\phi_j} J[\phi_1,\phi_2,\cdots,\phi_{N_f}](\mathbf{x})$ is given by (36). A proper reinitialization process should be applied to keep the sign-distance property [16, 44] during the evolution, which is an important step to regularize the solution of the level-set equation.

iii. Finally, the internal source is given $f^*(\mathbf{x}) = \sum_{j=1}^{N_f} f_j H(\phi_j^*(\mathbf{x}))$.

Once the source is recovered, we will use it to help with the inversion of the velocity. However, due to the ill-posedness of this inverse problem, only sufficiently accurate sources can be used. Otherwise, the accumulated error in the source function may significantly impact the inversion of the velocity. In order to avoid such instability, we will assume that the velocity $c(\mathbf{x})$ is piecewise constant with known support, namely $c^2 = c_0^2 + \sum_{j=1}^{N_c} c_j^2 \chi(\Omega_{c_j})$, where the subdomains Ω_{c_j}'s are known, and it remains to compute the amplitudes Ω_{c_j}. We solve this problem using a waveform fitting process in the least-squares sense:

$$\min_{\delta v_j} J_v[v_1, v_2, \cdots, v_{N_r}] = \min_{\delta v_j} \frac{1}{2}\int_0^T \int_{\partial\Omega} |\hat{u}(\mathbf{z},t) - \hat{d}(\mathbf{z},t)|^2 \mathrm{d}s_{\mathbf{z}}\mathrm{d}t, \tag{39}$$

where $\hat{u}(\mathbf{x}_r,t)$ is the simulated data using the reconstructed source $f(\mathbf{x})$ and $d(\mathbf{x}_r,t)$ is the measured scattering data.

4 Numerical Examples

We present numerical examples in 2D and 3D based on the proposed reconstruction methods for piecewise constant sources. In certain cases, we will reconstruct the piecewise constant velocities as well. However, reconstruction of velocities is generally more ill-posed than reconstruction of sources, and thus it poses more challenges for numerical experiments.

4.1 Forward Data Generation

We simulate the acoustic wave propagation (1)–(2) with the MATLAB k-wave toolbox [46] to generate the temporal boundary data (3). The k-wave toolbox solves the following first order system of equations using the first order k-space pseudo-spectral method:

$$\begin{cases} \frac{1}{c^2(\mathbf{x})}\frac{\partial p(t,\mathbf{x})}{\partial t} = -\rho\nabla_{\mathbf{x}}\cdot q(t,\mathbf{x}), \\ \frac{\partial q(t,\mathbf{x})}{\partial t} = -\frac{1}{\rho}\nabla_{\mathbf{x}} p(t,\mathbf{x}), \\ p|_{t=0} = p_0(\mathbf{x}), \\ q|_{t=0} = 0. \end{cases}$$

Here $p(t,\mathbf{x})$ is the acoustic pressure field, $q(t,\mathbf{x})$ is the acoustic particle velocity, ρ_0 is the ambient density, $c(\mathbf{x})$ is the SOS, and $p_0(\mathbf{x})$ is the initial pressure field. This first order system can be reduced to the usual second-order acoustic wave equation for p:

$$\begin{cases} \frac{1}{c^2(\mathbf{x})}\frac{\partial^2 p(t,\mathbf{x})}{\partial t^2} - \rho\nabla_{\mathbf{x}}\cdot\frac{1}{\rho}\nabla_{\mathbf{x}} p(t,\mathbf{x}) = 0 \quad \text{in } (0,+\infty)\times\mathbb{R}^d, \\ p(0,\mathbf{x}) = p_0(\mathbf{x}), \\ \frac{\partial p}{\partial t}(0,\mathbf{x}) = 0. \end{cases} \tag{40}$$

When the ambient density ρ is constant, this is the PAT/TAT model (28). We will take $\rho \equiv 1$ from now on.

In view of the connection between our problem and PAT/TAT (see Remark 1), we first take $p_0(\mathbf{x}) = c^2(\mathbf{x})f(\mathbf{x})$ to generate the pressure data $p(t,\mathbf{x})$ and the particle velocity data $q(t,\mathbf{x})$, and then compute the integral $\partial_t^{-1}p(t,\mathbf{x}) := \int_0^t p(\tau,\mathbf{x})\,\mathrm{d}\tau$ (which is $\hat{v}$ in (30)). The measurable boundary data and boundary gradient data are

$$\partial_t^{-1}p(t,\mathbf{x}), \qquad \nabla_{\mathbf{x}}\partial_t^{-1}p(t,\mathbf{x}) = -q(t,\mathbf{x}), \qquad \mathbf{x}\in\partial\Omega.$$

In order to apply our reconstruction methods, we take the Fourier transform of the temporal data to obtain the frequency domain data at a fixed low frequency $\omega_0 > 0$:

$$\int_0^T \partial_t^{-1}p(\tau,\mathbf{x})\mathrm{e}^{\mathbf{i}\omega_0\tau}\mathrm{d}\tau = -\frac{1}{\mathbf{i}\omega_0}\int_0^T p(\tau,\mathbf{x})\mathrm{e}^{\mathbf{i}\omega_0\tau}\mathrm{d}\tau, \qquad -\int_0^T q(\tau,\mathbf{x})\mathrm{e}^{\mathbf{i}\omega_0\tau}\mathrm{d}\tau, \qquad \mathbf{x}\in\partial\Omega,$$

where $T > 0$ is sufficiently large to ensure minimum acoustic energy trapped in the domain Ω. This is the simulated forward data utilized in our numerical inversion.

4.2 Accuracy of the First Term

To begin with, we verify the accuracy of the zero order approximation in 2D. We use three different SOS models, as shown in Figs. 1a–c, along with the same source function $f(\mathbf{x})$, as shown in Fig. 2a, to demonstrate that the first term $u_0(\mathbf{x})$ is independent of the chosen velocity model and hence only contains the source information.

The two dimensional computational domain is $\Omega = [-115, 115]\times[-115, 115]$ mm^2 with a spacing of 1 mm. The reference background SOS is $c_0 = 1\,500$ m/s. We take $T = 6$ milliseconds as the total propagation time to avoid any significant energy present in the computational domain. The time sampling rate is $\Delta t = 10^{-4}$ milliseconds. A total of 128

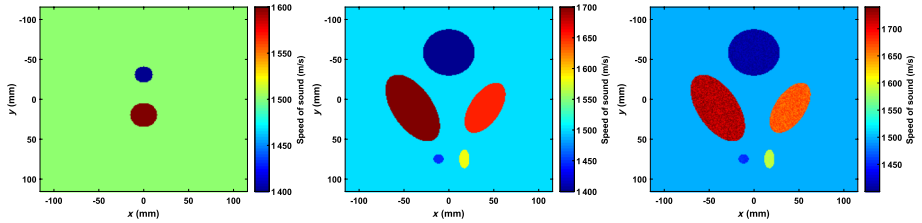

Fig. 1 The speed of sound models: **a** two disks; **b** shepp-Logan phantom like with piecewise constant velocities; **c** shepp-Logan phantom like with random velocities

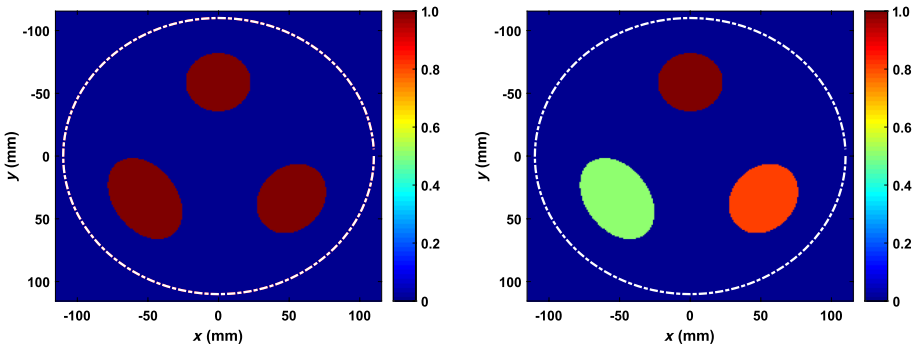

Fig. 2 The internal source models overlapped with the sensors: **a** an equal amplitude and **b** variable amplitudes

sensors are placed along a circle of radius 110 mm centered at the origin to measure the time-domain scattering data. We choose 100 Hz as the lowest frequency, i.e., the angular frequency $\omega_0 = 2\pi \times 100$, to approximate the zero frequency data.

Figures 3a and 3b display the x- and y-components of the true gravimetry data (computed via (15)) and the scattering data at 100 Hz for the three different SOS models. We can see that the approximate low-frequency data from three SOS models are almost the same as the true gravimetry data. The relative L^2-error is about 0.6% for each component. This validates that the quantity $\nabla_{\mathbf{x}} u_0(\mathbf{x})$ does not depend on the SOS model and encodes only information of the source $f(\mathbf{x})$.

4.3 Two-dimensional Examples

Case 1 Source with Equal Amplitudes.

Source Inversion Once the accuracy of the low frequency data is verified, we are ready to reconstruct the source. We apply the level set method to solve the inverse problem of gravimetry (15). Figure 4a shows the initial guess of the zero level-set function (blue dotted line) overlapped with the zero level-set of the target source (red solid). We plot the zero level-set function generated by the fast local level-set method [18, 31, 32] at the 400th evolution step in Fig. 4a. We observe that the reconstructed zero level-set function (blue

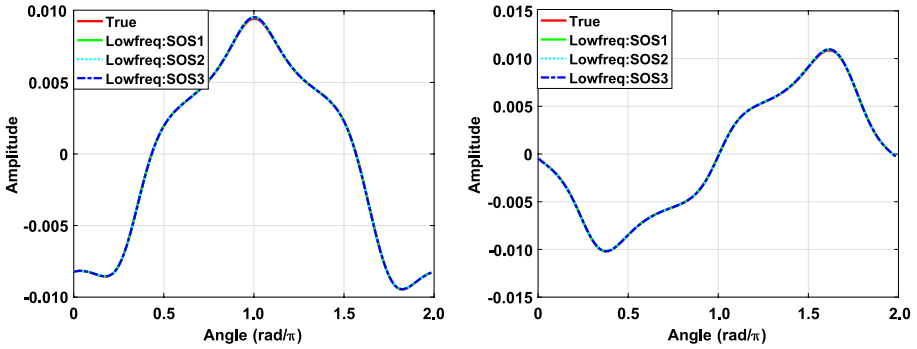

Fig. 3 Comparisons of the true gravimetry data generated via (15) and the low frequency approximation $\nabla u(\mathbf{x}, \omega_0)$ at 100 Hz for three different SOS models in Figs. 1**a**–1**c**. **a** x-component and **b** y-component

dotted line) successfully converges to the jumps of the target source rapidly, and the corresponding simulated data with the reconstructed level-set function can match both x- and y-components of the low frequency data very well, as is shown in Fig. 4b. This indicates that our method has effectively resolved the support of the internal source by using only the low frequency data without knowing the velocity as a prior.

Velocity Inversion Due to the nonlinearity of the velocity inversion, the error in the source term (either in the amplitude or the support) can severely impact the reconstruction of the velocity based on our numerical experiences. To reduce such impact, we take the SOS model to be piecewise constant with known jump discontinuities and focus on reconstruction of the amplitudes. Due to the severe ill-posedness of the problem, we know this may not be applied to all the scenarios in practice. Further research is needed to extend our algorithm to reconstruct more general velocity in a practical way.

We perform the inversion of the SOS amplitudes in the frequency domain by the data fitting criteria based on the least-squares objective (39), which is optimized by the L-BFGS algorithm. The data frequency band is from 60 kHz to 90 kHz and a constant value of 1 500 m/s is used as the initial guess for the inversion of SOS. The reconstructions at the 9th iteration and the 20th iteration for the first and second SOS models are shown in Fig. 5a and Fig. 5b, respectively. The corresponding SOS target amplitudes and reconstructed amplitudes are summarized in Table 1, where small relative errors are observed. One interesting point worth mentioning is that larger errors appear in the subdomain with a smaller size in both cases, which is an indication that some proper pre-conditioners should be applied so that the updating direction remains fair for subdomains with different sizes.

Case 2 Source with Variable Amplitudes.

Source Inversion In this case, we reconstruct a piecewise constant source function $f(\mathbf{x})$ with variable amplitudes. The initial guess of the zero level set is the same as shown in Fig. 6a, yet with three amplitudes 0.8, 0.5, and 1, respectively, on the subdomains. This is plotted in Fig. 6a. After 1 120 evolution steps, the reconstructed source is displayed in Fig. 6b and its zero level-set function in Fig. 7a. We also compare two components of the simulated data by the reconstructed source in Fig. 7b, which shows that the data match almost perfectly. These results validate that our source inversion method is effective in reconstructing sources with high precision.

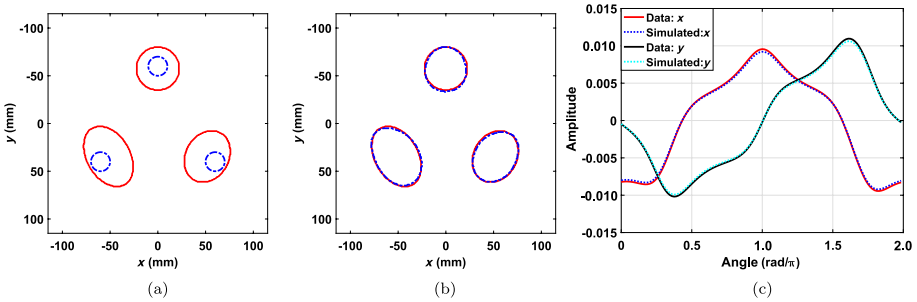

Fig. 4 **a** The initial zero level-set function and **b** the reconstructed zero level-set function overlapped with the true level-set function at the 400th iteration. **c** Comparisons of x- and y-components of the simulated data by the inverted level-set function and the measured data

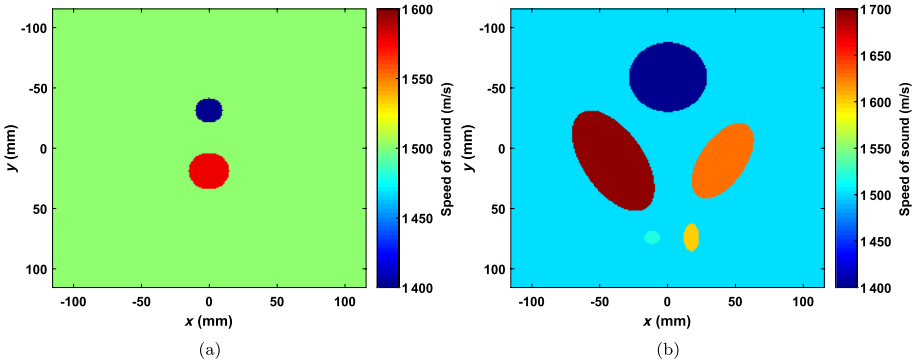

Fig. 5 Reconstructed piecewise constant SOS values with given supports of SOS models: **a** two-disk model and **b** shepp-Logan phantom like model

Table 1 Comparison of the target SOS values and the reconstructed SOS values in the first and second SOS models

True v (m/s)	Inv. v (m/s)	Rel. error
1 400	1 367	2.36%
1 600	1 576	1.50%
1 400	1 402	0.14%
1 450	1 518	4.69%
1 580	1 600	1.33%
1 650	1 629	1.60%
1 700	1 694	0.35%

The larger relative errors are present in the subdomains of smaller sizes

Noisy Source Inversion Next, we study the source inversion with noisy data measurement. The noise added to the simulated data is Gaussian random noise with mean zero and standard

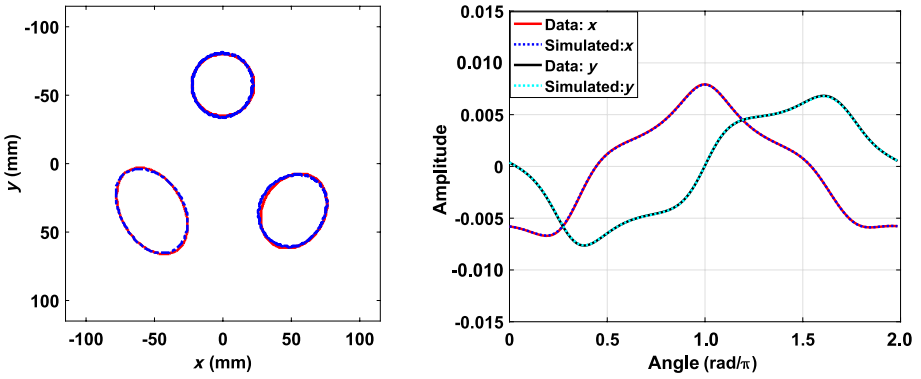

Fig. 6 Comparisons of **a** the initial guess and **b** the inverted source models at the 1 270th evolution step for the source inversion with variable amplitudes

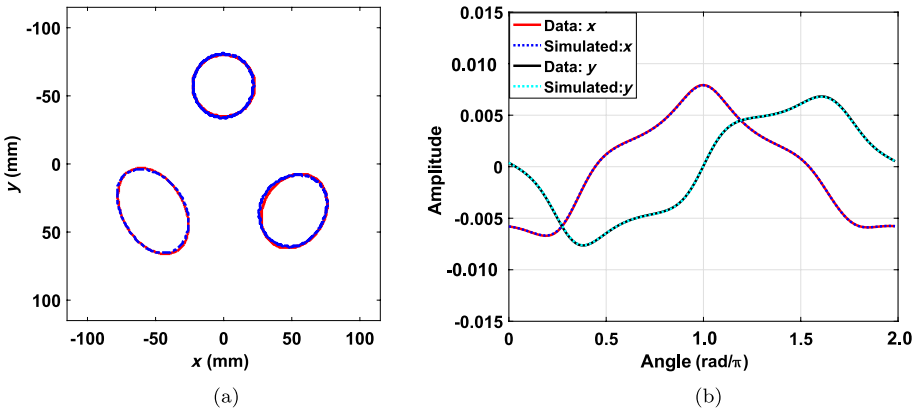

Fig. 7 **a** Reconstructed zero level-set function overlapped with the true level-set function at the 1 270th iteration. **b** Comparison of x- and y-components of the simulated data by the inverted level-set function and the measured data

deviation of the 2% maximum absolute value of the time-domain velocity data $q(t, \mathbf{x})$. We still extract the low-frequency data at 100 Hz by transforming the noisy data into the frequency domain as before. We start with the same initial level-set function as in Fig. 6a using the known amplitudes on each level-set function. The CFL number for the level-set evolution is decreased to 0.6 in this test to stabilize the inversion, which serves as a kind of regularization for the small step size used in the gradient descent method. The final result at the 1 690th evolution step is plotted in Fig. 8a overlapped with the target zero level-set function. See also Fig. 8a in comparison with Fig. 2b. We still can observe a good recovery of the support of the internal source in the case of noisy data. The simulated data by the inverted result are also very close to the measured noisy data as shown in Fig. 8b, which gives a relative data residual of 5.1% and 4.3% for the x- and y-components, respectively, indicating the successful reconstruction from the noisy data without any velocity information.

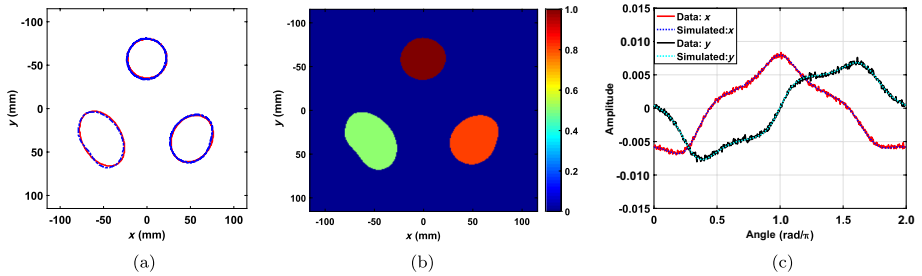

Fig. 8 Inversion with noisy data. **a** Zero level-set function overlapped with the true level-set function and **b** the reconstructed source models at the 1 310th evolution step. **c** Comparison of x- and y-components of the simulated data by the inverted level-set function and the measured data

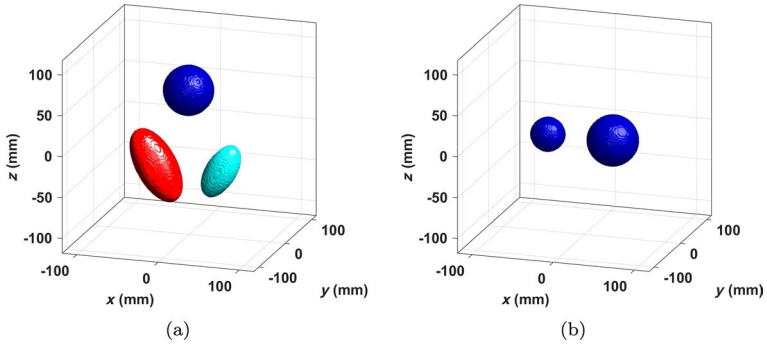

Fig. 9 Three dimensional example. **a** Speed of sound model and **b** the internal source

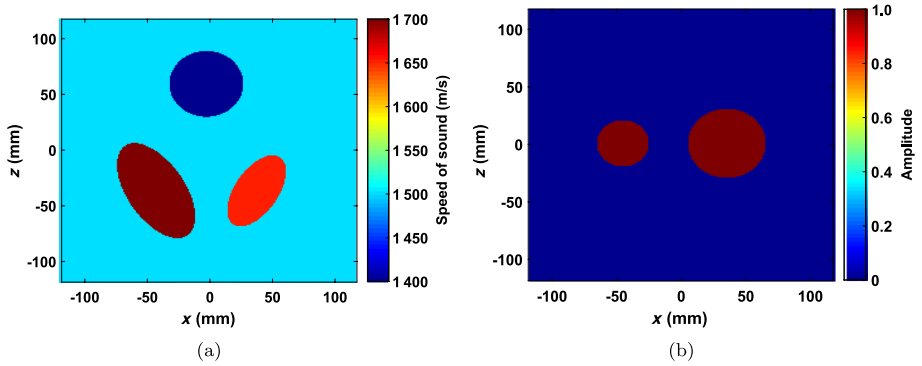

Fig. 10 Three dimensional example. Cross-section of **a** speed of sound model and **b** the internal source at $y = 0$ mm

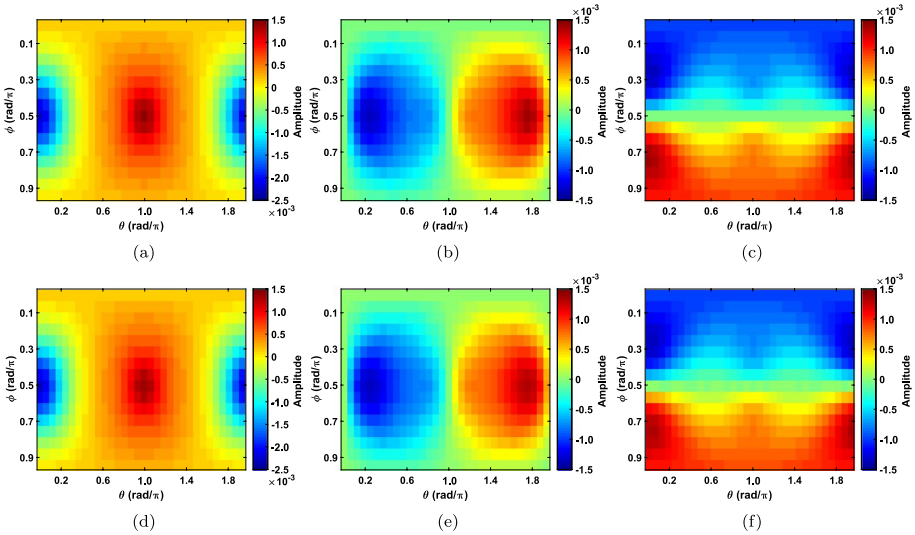

Fig. 11 Three dimensional example. Comparisons of the three components of **a**, **b**, **c** the low frequency approximation $\nabla u(\mathbf{x}, \omega_0)$ at 100 Hz and **d**, **e**, **f** true gravimetry data. The relative errors are respectively 0.93%, 0.93%, 0.83%

4.4 Three dimensional Examples

Source Inversion We now consider three dimensional inversion of the source function. The SOS model and the source model in this three dimensional experiment are plotted in Figs. 9a and 9b. The velocity model consists of three different values: 1 400 m/s, 1 600 m/s, 1 800 m/s, and the source amplitudes are of equal values on the two subdomains. The reference background SOS is $v_0 = 1\,500$ m/s. The cross-section of the SOS model and the source model at $y = 0$ mm are shown in Figs. 10a and 10b.

The computational domain in 3D is $[-128, 128] \times [-128, 128] \times [-128, 128]$ mm^3 with a spacing of 1 mm. As the wave energy in 3D decays faster than in 2D, we take $T = 0.34$ milliseconds as the total duration of wave propagation with a sampling rate of 1.7. A total of $32 \times 16 = 512$ sensors are placed on the surface of a sphere of radius of 100 mm centered at the origin to measure the scattering data.

In order to verify the accuracy of the low frequency approximation, we again choose 100 Hz as the lowest frequency to approximate the zero frequency data, i.e., $\omega_0 = 2\pi \times 100$ (rad/s). The low frequency data (real part) are shown in Figs. 11a–c in terms of its x-, y-, z-components. In comparison, the simulated gravimetry data using the exact source are plotted in Figs. 11d–f. All the data match very well, as is predicted by the theory.

For the inversion, we choose a spatial grid of size 2 mm on each direction and generate a mesh of $118 \times 118 \times 118$ to discretize the domain $[-118, 116] \times [-118, 116] \times [-118, 116]$ mm^3. The CFL number is 0.6 in this three dimensional example. We evolve the level-set equation to a steady state by starting with an initial guess that is a sphere centered at the origin with a radius of 50 mm; see Fig. 12a. Figure 12b shows the reconstructed zero level-set function at the 780th evolution step. Compared with the target source model in Fig. 9b, no significant difference is observed. Figure 12c displays the cross-section of the initial guess, the reconstructed source, and the target ground-truth source at $y = 0$ mm, which further confirms the accuracy

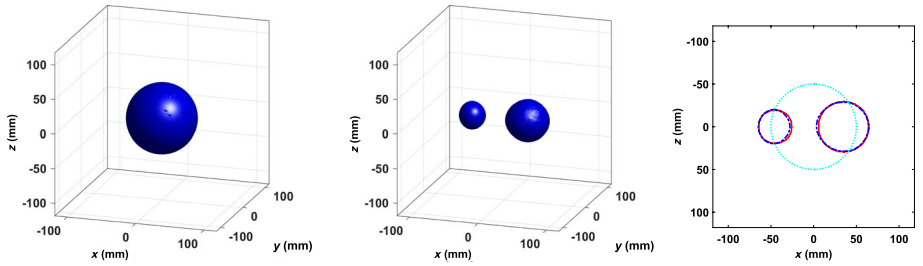

Fig. 12 Three dimensional example. **a** Initial guess and **b** reconstructed level-set function at the 780th evolution step

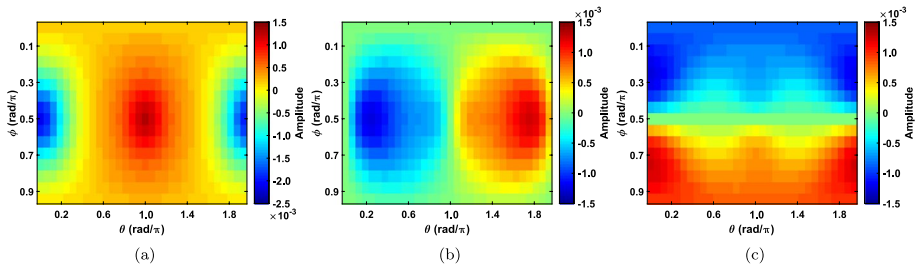

Fig. 13 Three dimensional example. **a**, **b**, **c** The x, y, z-components of the simulated data using the inverted source function at the 780th evolution step. The relative error is roughly 3% for each component

of the source inversion. We also re-simulated the gravimetry data using the reconstructed source as shown in Figs. 13a–c, which match very well with the measured low frequency data as shown in Figs. 11a–c, with the maximum relative error of only 3%.

Noisy Source Inversion To simulate the noisy data, we add the Gaussian random noise to the clean measurement. The noise has zero mean and a standard deviation of 2% of the maximum absolute value of the time-domain velocity data $q(t, \mathbf{x})$. The noisy data are then transformed to the frequency domain to yield the low-frequency data at 100 Hz. The initial level-set function is again the sphere in Fig. 12a, and all the other parameters are the same as in the noise-free experiment. The level set evolution is terminated at the 1 690th step, as is shown in Fig. 14a, and the reconstructed cross-section at $y = 0$ mm overlapped with the target zero level-set function is plotted in Fig. 14b. The relative error is 17.3%, 12.9%, and 12.8% for each component, respectively, as is shown in Figs. 15a–f. It is clear that, in the presence of noise, our inversion method can still provide a reasonable reconstruction within an acceptable precision. Due to the fast decay of the wave field in 3D, the level-set method seems more sensitive to the random noise. One possible way to mitigate this effect is to apply the Kantorovich-Rubinstein norm in the inverse problem of gravimetry, which is more robust against random noise. We refer readers to the recent study [13, 14] for details.

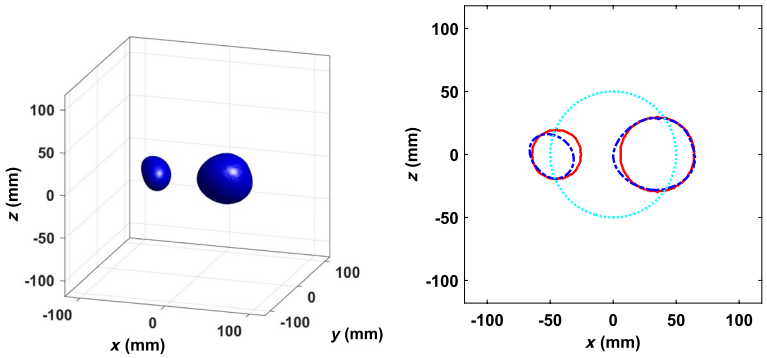

Fig. 14 Three dimensional example. Comparisons of the zero-level of the target model (red solid) and initial guess (cyan) and the inverted model at the 1 690 th evolution step

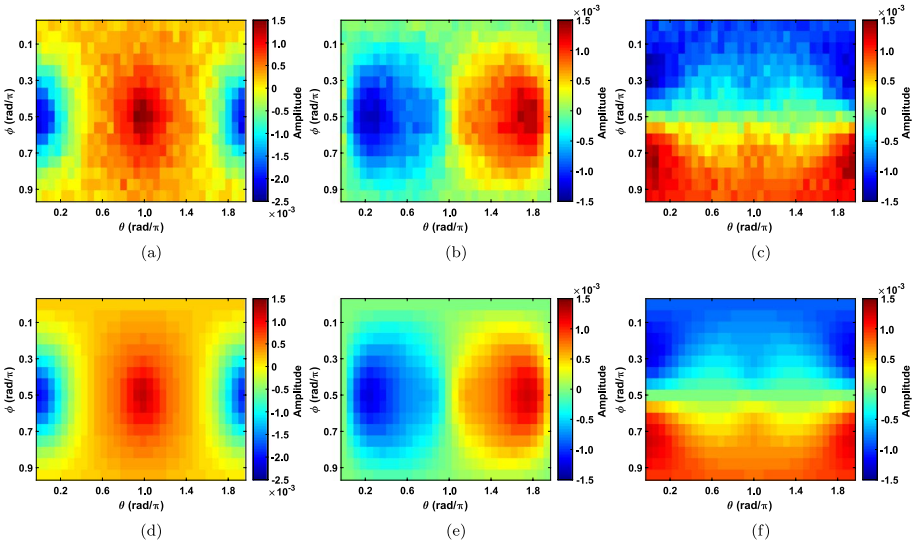

Fig. 15 Three dimensional example. **a**, **b**, **c** are the *x*-, *y*-, *z*-components of the simulated data using the inverted source function at the 780th evolution step. The relative error is roughly 3% for each component

5 Conclusion

We investigated the reconstruction of a piecewise constant passive acoustic source from a single boundary temporal measurement without knowing the speed of sound and proved some related theoretical uniqueness results. Numerical examples validated our proposed methodology. Generalizing this setup to elastic waves consists of ongoing work.

Acknowledgements We would like to acknowledge Michigan State University HPCC for providing the computational resources that contributed to the research results reported here. Qian is partially supported by the NSF (Grant Nos. 2012046, 2152011, and 2309534). Yang is partially supported by the NSF (Grant Nos.

DMS-1715178, DMS-2006881, and DMS-2237534), NIH (Grant No. R03-EB033521), and startup fund from Michigan State University.

Compliance with Ethical Standards

Conflict of Interest On behalf of all authors, the corresponding author states that there is no conflict of interest.

References

1. Acosta, S.: Recovery of pressure and wave speed for photoacoustic imaging under a condition of relative uncertainty. Inverse Problems **35**(11), 115013 (2019)
2. Agranovsky, M., Kuchment, P.: Uniqueness of reconstruction and an inversion procedure for thermoacoustic and photoacoustic tomography with variable sound speed. Inverse Problems **23**(5), 2089 (2007)
3. Arridge, S.R., Betcke, M.M., Cox, B.T., Lucka, F., Treeby, B.E.: On the adjoint operator in photoacoustic tomography. Inverse Problems **32**(11), 115012 (2016)
4. Bao, G., Lin, J., Triki, F.: A multi-frequency inverse source problem. J. Differential Equations **249**(12), 3443–3465 (2010)
5. Belhachmi, Z., Glatz, T., Scherzer, O.: A direct method for photoacoustic tomography with inhomogeneous sound speed. Inverse Problems **32**(4), 045005 (2016)
6. Chung, E., Lam, C.Y., Qian, J.: A Neumann series based method for photoacoustic tomography on irregular domains. Contemporary Mathematics **615**, 89–104 (2014)
7. Colton, D.L., Kress, R., Kress, R.: Inverse Acoustic and Electromagnetic Scattering Theory, vol. 93. Springer, New York (1998)
8. Finch, D., Hickmann, K.S.: Transmission eigenvalues and thermoacoustic tomography. Inverse Problems **29**(10), 104016 (2013)
9. Glowinski, R., Leung, S., Qian, J.: A penalization-regularization-operator splitting method for Eikonal-based traveltime tomography. SIAM J. Imaging Sci. **8**, 1263–1292 (2015)
10. Herglotz, G.: Über die analytische Fortsetzung des Potentials ins Innere der anziehenden Massen, volume 44. Teubner (1914)
11. Hristova, Y., Kuchment, P., Nguyen, L.: Reconstruction and time reversal in thermoacoustic tomography in acoustically homogeneous and inhomogeneous media. Inverse Problems **24**(5), 055006 (2008)
12. Huang, C., Wang, K., Schoonover, R.W., Wang, L.V., Anastasio, M.A.: Joint reconstruction of absorbed optical energy density and sound speed distributions in photoacoustic computed tomography: a numerical investigation. IEEE Transact. Comput. imaging **2**(2), 136–149 (2016)
13. Huang, G., Qian, J.: Analysis of Kantonovich-Rubinstein norm and its application to inverse gravity problem. SIAM J. Imaging Sci. **12**(3), 1528–1560 (2019)
14. Huang, G., Zhang, X., Qian, J.: Kantorovich-Rubinstein misfit for inverting gravity-gradient data by the level-set method. Geophysics **84**(5), G55–G73 (2019)
15. Isakov, V.: Inverse Source Problems. American Mathematical Society, Providence, Rhode Island (1990)
16. Isakov, V.: Inverse Problems for Partial Differential Equations, vol. 127. Springer, New York (2006)
17. Isakov, V., Leung, S., Qian, J.: A fast local level set method for inverse gravimetry. Comm. Comput. Phys. **10**, 1044–1070 (2011)
18. Isakov, V., Leung, S., Qian, J.: A three-dimensional inverse gravimetry problem for ice with snow caps. Inverse Prob. Imaging **7**, 523–544 (2013)
19. Ishii, M., Shearer, P.M., Houston, H., Vidale, J.E.: Extent, duration and speed of the 2004 Sumatra-Andaman earthquake imaged by the Hi-Net array. Nature **435**(7044), 933–936 (2005)
20. Johnson, R.L., Scott, M.P., Jeffrey, R.G., Chen, Z., Bennett, L., Vandenborn, C., Tcherkashnev, S.: Evaluating hydraulic fracture effectiveness in a coal seam gas reservoir from surface tiltmeter and microseismic monitoring. In: SPE Annual Technical Conference and Exhibition. OnePetro (2010)
21. Knox, C., Moradifam, A.: Determining both the source of a wave and its speed in a medium from boundary measurements. Inverse Problems **36**(2), 025002 (2020)

22. Leung, S., Qian, J.: An adjoint state method for three-dimensional transmission traveltime tomography using first-arrivals. Comm. Math. Sci. **4**, 249–266 (2006)
23. Leung, S., Qian, J., Hu, J.: A level-set adjoint-state method for transmission traveltime tomography in irregular domains. SIAM J. Sci. Comput. **43**, A2352–A2380 (2021)
24. Li, W., Leung, S., Qian, J.: A level set-adjoint state method for crosswell transmission-reflection traveltime tomography. Geophys. J. Internat. **199**, 348–367 (2014)
25. Li, W., Lu, W., Qian, J.: A level set method for imaging salt structures using gravity data. Geophysics **81**(2), G35–G51 (2016)
26. Li, W., Lu, W., Qian, J., Li, Y.: A multiple level set method for three-dimensional inversion of magnetic data. Geophysics **82**(5), J61–J81 (2017)
27. Li, W., Qian, J.: Joint inversion of gravity and traveltime data using a level-set based structural parameterization. Geophysics **81**(6), G107–G119 (2016)
28. Li, W., Qian, J.: Simultaneously recovering both domain and varying density in inverse gravimetry by efficient level-set methods. Inverse Prob. Imaging **15**, 387–413 (2021)
29. Li, W., Qian, J.: Kantorovich-Rubinstein metric based level-set methods for inverting modulus of gravity-force data. Inverse Prob. Imaging **16**, 1643–1667 (2022)
30. Liu, H., Uhlmann, G.: Determining both sound speed and internal source in thermo- and photo-acoustic tomography. Inverse Problems **31**(10), 105005 (2015)
31. Lu, W., Leung, S., Qian, J.: An improved fast local level set method for three-dimensional inverse gravimetry. Inverse Prob. Imaging **9**, 479–509 (2015)
32. Lu, W., Qian, J.: A local level set method for three-dimensional inversion of gravity gradiometry data. Geophysics **80**, G35–G51 (2015)
33. Matthews, T.P., Poudel, J., Li, L., Wang, L.V., Anastasio, M.A.: Parameterized joint reconstruction of the initial pressure and sound speed distributions for photoacoustic computed tomography. SIAM J Imaging Sci. **11**(2), 1560–1588 (2018)
34. Osher, S.J., Fedkiw, R.: Level Set Methods and Dynamic Implicit Surfaces. Springer, New York (2003)
35. Osher, S.J., Sethian, J.A.: Fronts propagating with curvature dependent speed: algorithms based on Hamilton-Jacobi formulations. J. Comput. Phys. **79**, 12–49 (1988)
36. Osher, S.J., Shu, C.-W.: High-order essentially nonoscillatory schemes for Hamilton-Jacobi equations. SIAM J. Numer. Anal. **28**, 907–922 (1991)
37. Qian, J., Stefanov, P., Uhlmann, G., Zhao, H.: An efficient Neumann series-based algorithm for thermoacoustic and photoacoustic tomography with variable sound speed. SIAM J. Imag. Sci. **4**(3), 850–883 (2011)
38. Qin, S., Yang, Y., Wang, R.: Source independent velocity recovery using imaginary FWI. In: 82nd EAGE Annual Conference & Exhibition, vol. 2021, pp. 1–5. European Association of Geoscientists & Engineers (2021)
39. Shan, H., Wiedeman, C., Wang, G., Yang, Y.: Simultaneous reconstruction of the initial pressure and sound speed in photoacoustic tomography using a deep-learning approach. In: Novel Optical Systems, Methods, and Applications XXII, vol. 11105, pp. 1110504. International Society for Optics and Photonics (2019)
40. Sharan, S., Wang, R., Herrmann, F.J.: Fast sparsity-promoting microseismic source estimation. Geophys. J. Int. **216**(1), 164–181 (2019)
41. Stefanov, P., Uhlmann, G.: Thermoacoustic tomography with variable sound speed. Inverse Problems **25**(7), 075011 (2009)
42. Stefanov, P., Uhlmann, G.: Instability of the linearized problem in multiwave tomography of recovery both the source and the speed. arXiv:1211.6217 (2012)
43. Sun, J., Xue, Z., Zhu, T., Fomel, S., Nakata, N.: Full-waveform inversion of passive seismic data for sources and velocities. In: SEG Technical Program Expanded Abstracts 2016, pp. 1405–1410. Society of Exploration Geophysicists (2016)
44. Sussman, M., Smereka, P., Osher, S.J.: A level set approach for computing solutions to incompressible two-phase flows. J. Comput. Phys. **114**, 146–159 (1994)
45. Tick, J., Pulkkinen, A., Tarvainen, T.: Modelling of errors due to speed of sound variations in photoacoustic tomography using a Bayesian framework. Biomed. Phys. Eng. Express **6**(1), 015003 (2019)
46. Treeby, B.E., Cox, B.T.: k-wave: Matlab toolbox for the simulation and reconstruction of photoacoustic wave fields. J. Biomed. Optics **15**(2), 021314 (2010)
47. Van den Doel, K., Ascher, U.M., Leitao, A.: Multiple level sets for piecewise constant surface reconstruction in highly ill-posed problems. J. Sci. Comput. **43**(1), 44–66 (2010)

48. Wang, H., Alkhalifah, T.: Microseismic imaging using a source function independent full waveform inversion method. Geophys. J. Int. **214**(1), 46–57 (2018)
49. Wang, K., Anastasio, M.A.: Photoacoustic and thermoacoustic tomography: image formation principles. In: Handbook of Mathematical Methods in Imaging. Springer, New York (2015)
50. Wang, L.V., Wu, H.-I.: Biomedical Optics: Principles and Imaging. Wiley-Interscience, New Jersey (2007)
51. Xia, J., Yao, J., Wang, L.V.: Photoacoustic tomography: principles and advances. Electromagnetic Waves (Cambridge Mass.) **147**, 1–22 (2014)
52. Xu, M., Wang, L.V.: Photoacoustic imaging in biomedicine. Rev. Sci. Instrum. **77**(4), 041101 (2006)
53. Ye, M., Cao, M., Feng, T., Yuan, J., Cheng, Q., Liu, X., Xu, G., Wang, X.: Automatic speed of sound correction with photoacoustic image reconstruction. Photons Plus Ultrasound **9708**, 601–606 (2016)
54. Yoon, C., Kang, J., Han, S., Yoo, Y., Song, T.-K., Chang, J.H: Enhancement of photoacoustic image quality by sound speed correction: ex vivo evaluation. Optics Express **20**(3), 3082–3090 (2012)
55. Zhang, J., Wang, K., Yang, Y., Anastasio., M.A.: Simultaneous reconstruction of speed-of-sound and optical absorption properties in photoacoustic tomography via a time-domain iterative algorithm. In: Photons Plus Ultrasound: Imaging and Sensing 2008: the Ninth Conference on Biomedical Thermoacoustics, Optoacoustics, and Acousto-optics, **6856**, pp. 68561F. International Society for Optics and Photonics (2008)